

Quantitative prediction of 3D solution shape and flexibility of nucleic acid nanostructures

Do-Nyun Kim¹, Fabian Kilchherr², Hendrik Dietz^{2*}, and Mark Bathe^{1*}

¹Laboratory for Computational Biology & Biophysics, Department of Biological Engineering,
Massachusetts Institute of Technology, Cambridge, MA, USA

²Department of Physics & Walter Schottky Institute, Center for Integrated Protein Science, Technische
Universität München, Garching, Germany

SUPPLEMENTARY DATA

(Supplementary Note 1 and Supplementary Figures 1-23)

SUPPLEMENTARY NOTE 1 – Single-stranded DNA

Single-stranded DNA connecting double-helical DNA domains is treated as an entropic spring with force-extension behavior described by the modified freely jointed chain model,

$$R = L \left[\coth \left(\frac{Fb}{k_B T} \right) - \frac{k_B T}{Fb} \right] \left(1 + \frac{F}{S} \right)$$

where R is end-to-end distance, L is contour length (0.56 nm times the number of bases), F is force, b is the Kuhn length (1.5 nm), which is equal to twice the persistence length, S is the stretch modulus (800 pN), k_B is the Boltzmann constant, and T is temperature, assumed to be 298 K (14). This model is implemented using a nonlinear truss finite element whose axial stress-strain relationship is directly derived from the above force-extension relationship as follows,

$$R_o(1 + \varepsilon) = L \left[\coth \left(\frac{\sigma b}{k_B T} \right) - \frac{k_B T}{\sigma b} \right] \left(1 + \frac{\sigma}{S} \right)$$

where R_o is initial length, ε is axial strain, and σ is axial stress in the truss element that is assumed to have unit cross-sectional area.

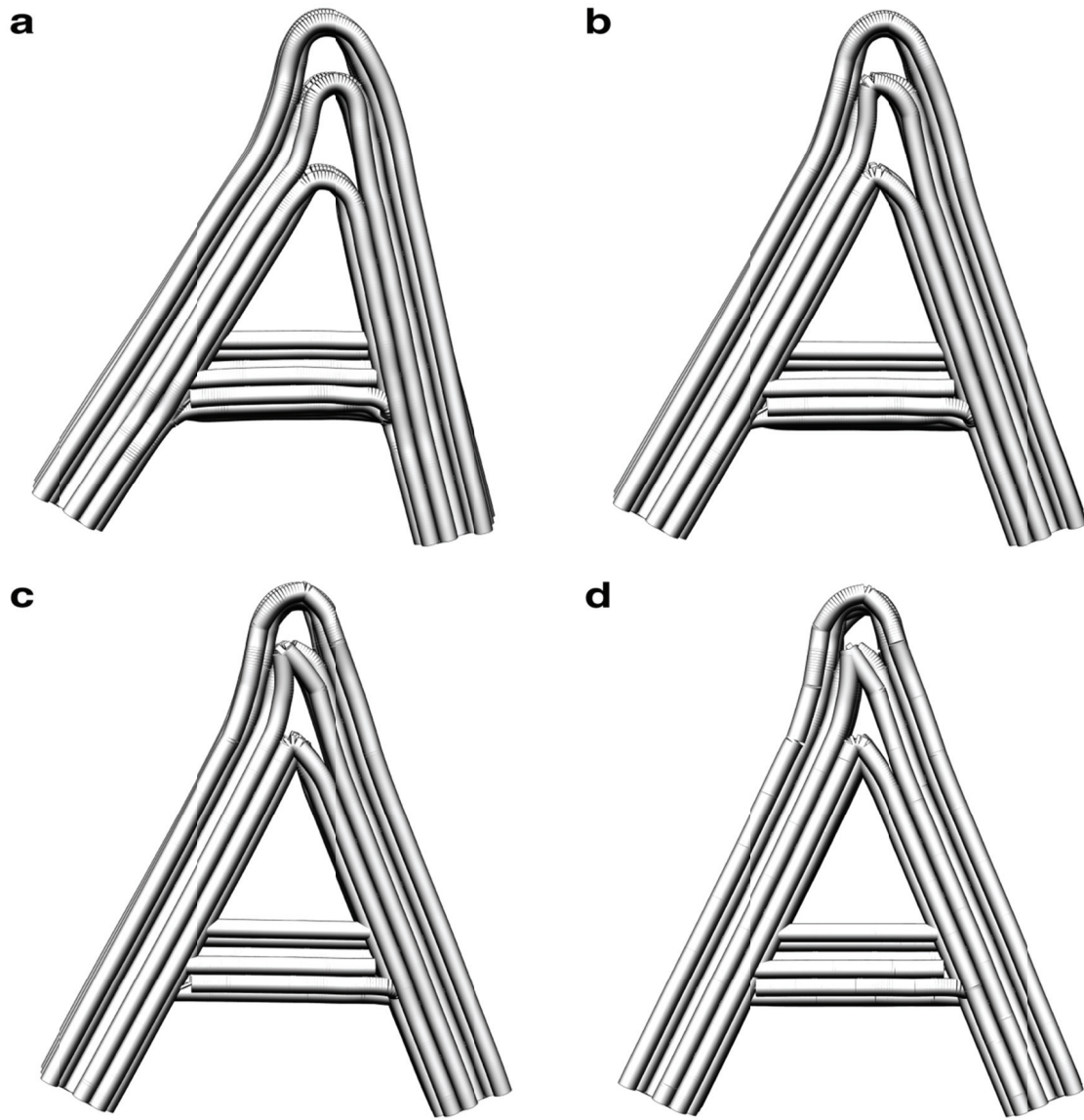


Figure S1 Effect of nick stiffness on the solution shape of an 'A'-like object. Backbone bending and torsional stiffness of nicks were reduced by a factor of (a) 1 (no reduction), (b) 10, (c) 100, and (d) 1,000 whereas stretching stiffness is retained at double-helix values. Sharp corners observed in TEM data (Figure S4) could be reproduced by using the factor of 100 and lower values (c-d). Scaling analysis also suggests a value of 100 based on the base-stacking energy of DNA.

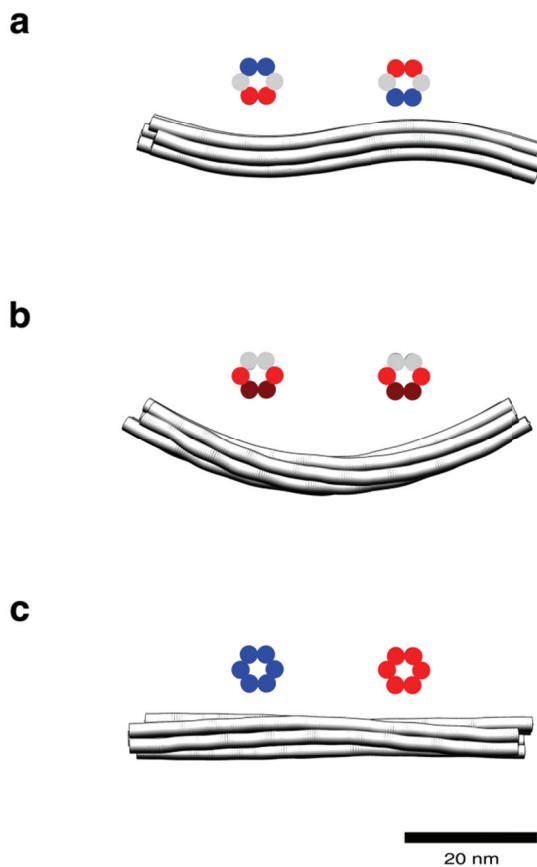


Figure S2 Example deformations of a honeycomb lattice bundle induced by insertion-deletion mismatch in neighboring DNA helices. Cross-sections represent the arrangement of insertions (red, 3 insertions) and deletions (blue, 3 deletions) for the left-half and right-half of each bundle along the helical axis. Dark red denotes helices with a higher density of insertions (6 insertions).

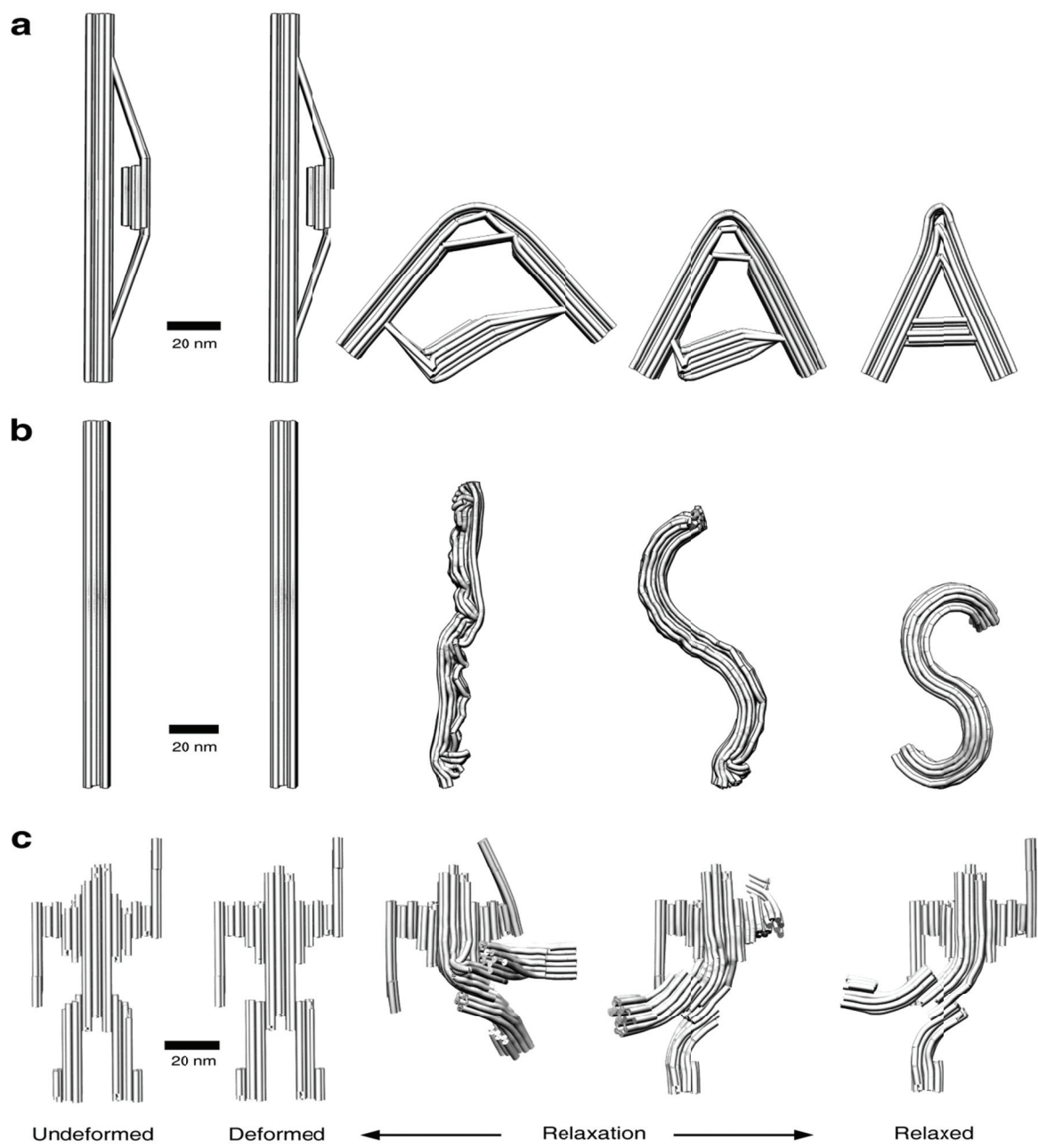


Figure S3 Snapshots of DNA origami structures during the deformation and relaxation processes.
(a) 'A'-like object, (b) 'S'-like object, and (c) robot-like object.

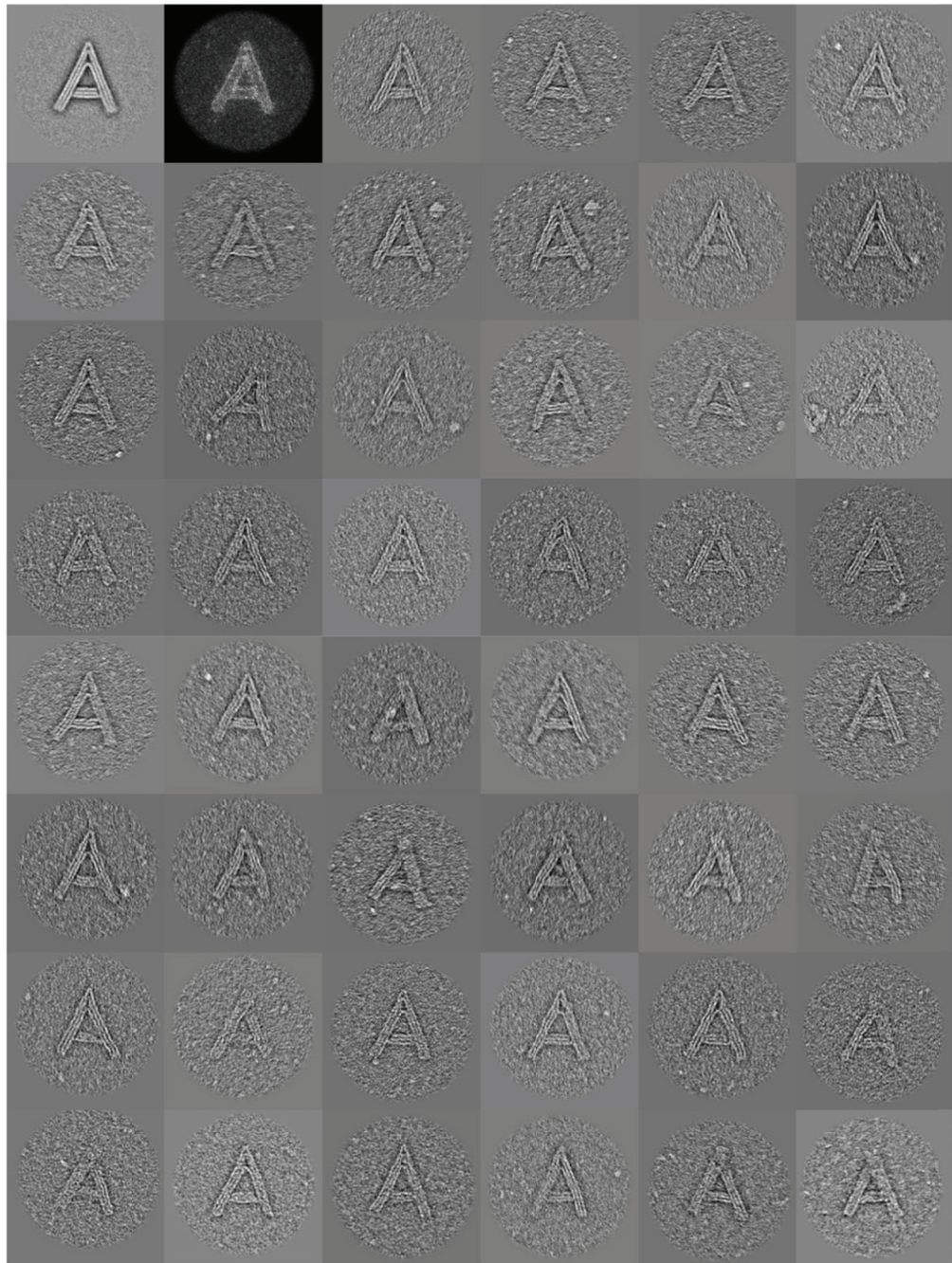


Figure S4 TEM images of ‘A’-like object. First two images correspond to mean and variance of 46 single particle images.

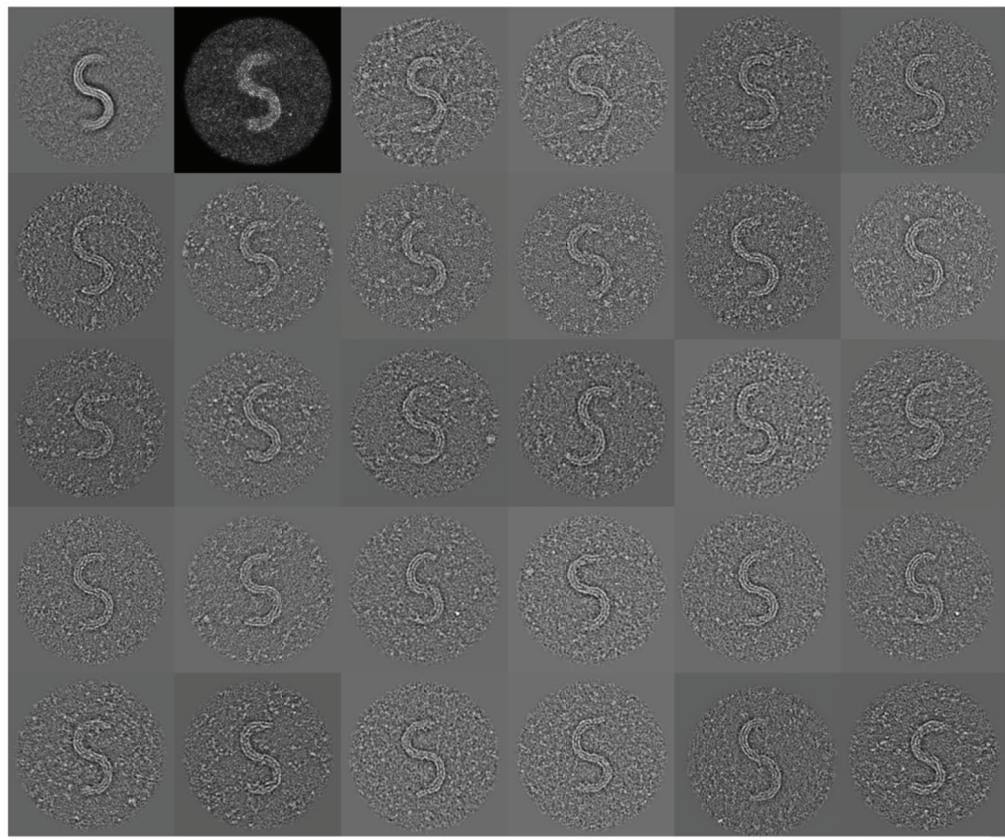
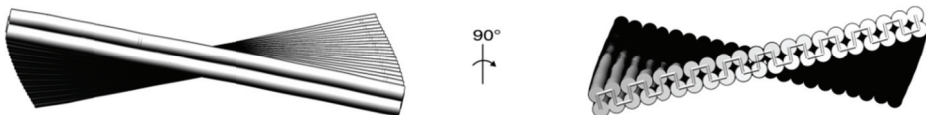


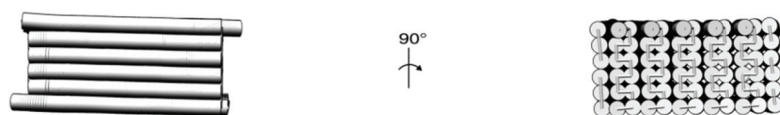
Figure S5 TEM images of ‘S’-like object. First two images correspond to mean and variance of 28 single particle images.

a

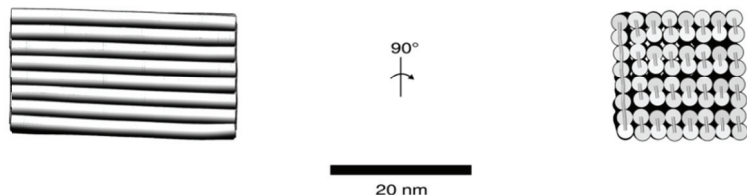
90°

b

90°

c

90°

d

20 nm

Figure S6 Multi-layer DNA origami blocks on a square lattice (21). Predicted 3D solution shapes of (a) two-layer, (b) three-layer, (c) six-layer, and (d) eight-layer blocks. Maximum crossover density is used in all designs.

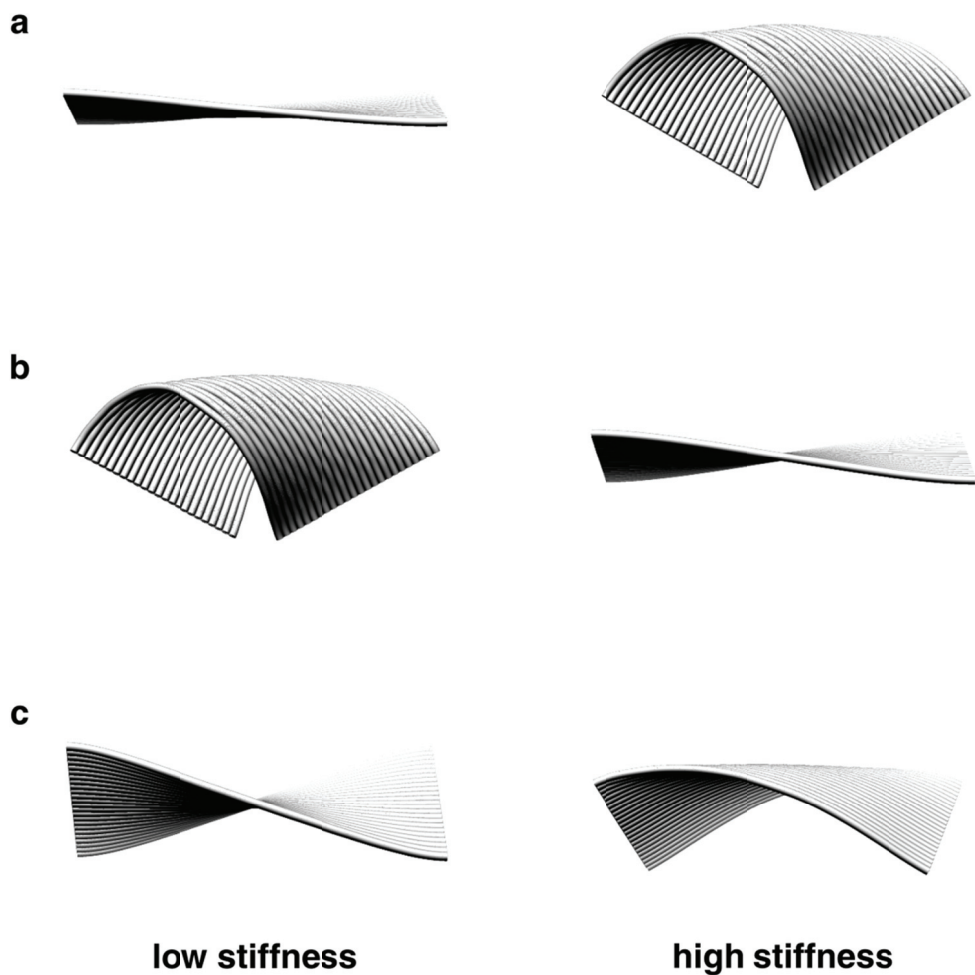


Figure S7 Investigation of twist-bend coupling observed in the single-layer DNA origami rectangle on a square lattice (5). 3D solution shapes are re-calculated for the rectangle assuming 10x higher/lower (a) twisting, (b) bending, and (c) stretching stiffness than default values of double-stranded DNA. Pure and minimal twisting of the rectangle is observed for low twisting stiffness in (a) because the torsional strain energy induced by the mismatch in crossover spacing (10.67 versus 10.5) in the square lattice is minimal, resulting in a nearly flat rectangle. In contrast, high twisting stiffness in (a) results in high initial torsional strain energy that is transferred to bending and stretching modes in the deformed shape. When bending stiffness is low in (b), the initial torsional strain energy results in a predominantly bent mode of the rectangle, whereas when bending stiffness is high in (b) the twisted rectangle again results. Finally, when stretching stiffness is low in (c) the rectangle exhibits a predominantly stretching mode of deformation where helices become progressively longer as external helices at the edges are approached from the central helix. In contrast, when stretching is prohibited by high stretching stiffness of the double-helix, the observed twisted-bent rectangle results. This analysis suggests that the twisted-bent shape of the single-layer DNA origami rectangle originates in a nonlinear stretch-bend-twist coupling.

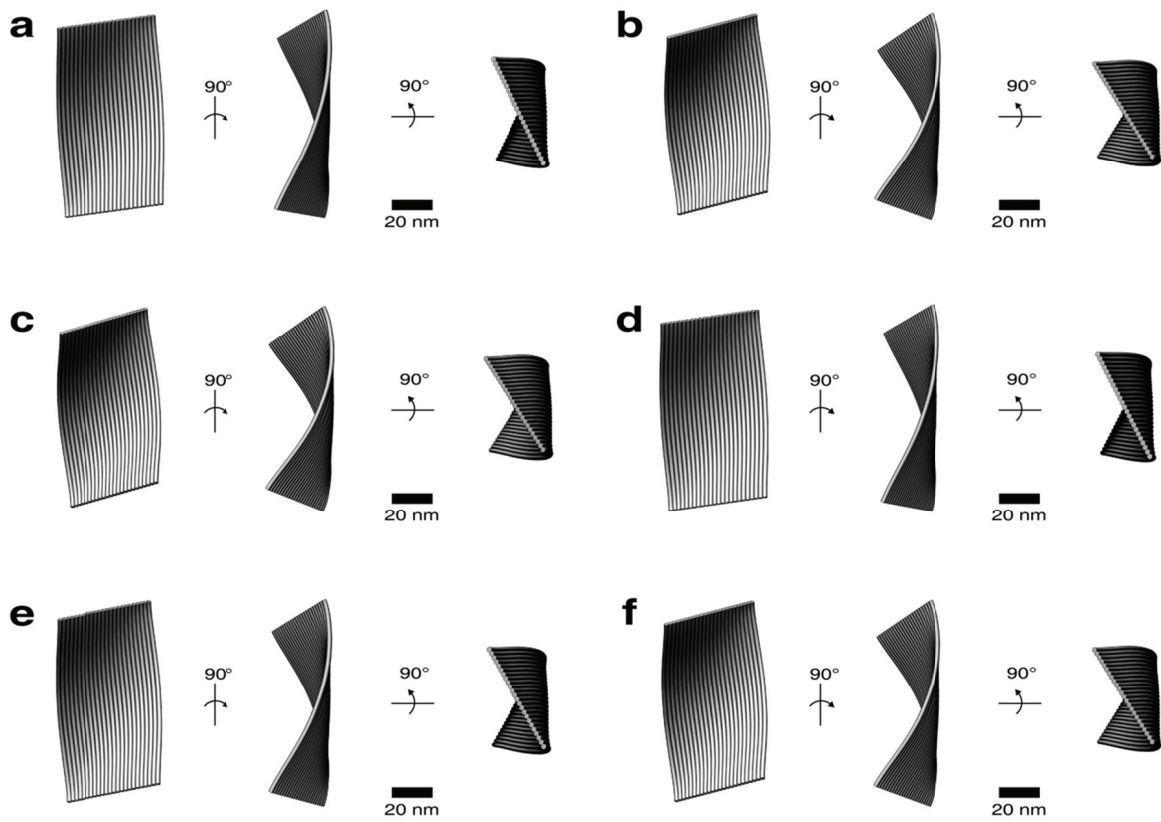


Figure S8 Sensitivity analysis of the single-layer DNA origami rectangle on a square lattice (5). 3D solution shapes are calculated by (a) 25% lower or (b) higher twisting stiffness, (c) 25% lower or (d) higher bending stiffness, and (e) 25% lower or (f) higher stretching stiffness than the default stiffness of double-stranded DNA. The overall bend in addition to twist are consistently observed, suggesting that the computed result is robust to variations in DNA double-helix stiffness observed experimentally (24, 25).

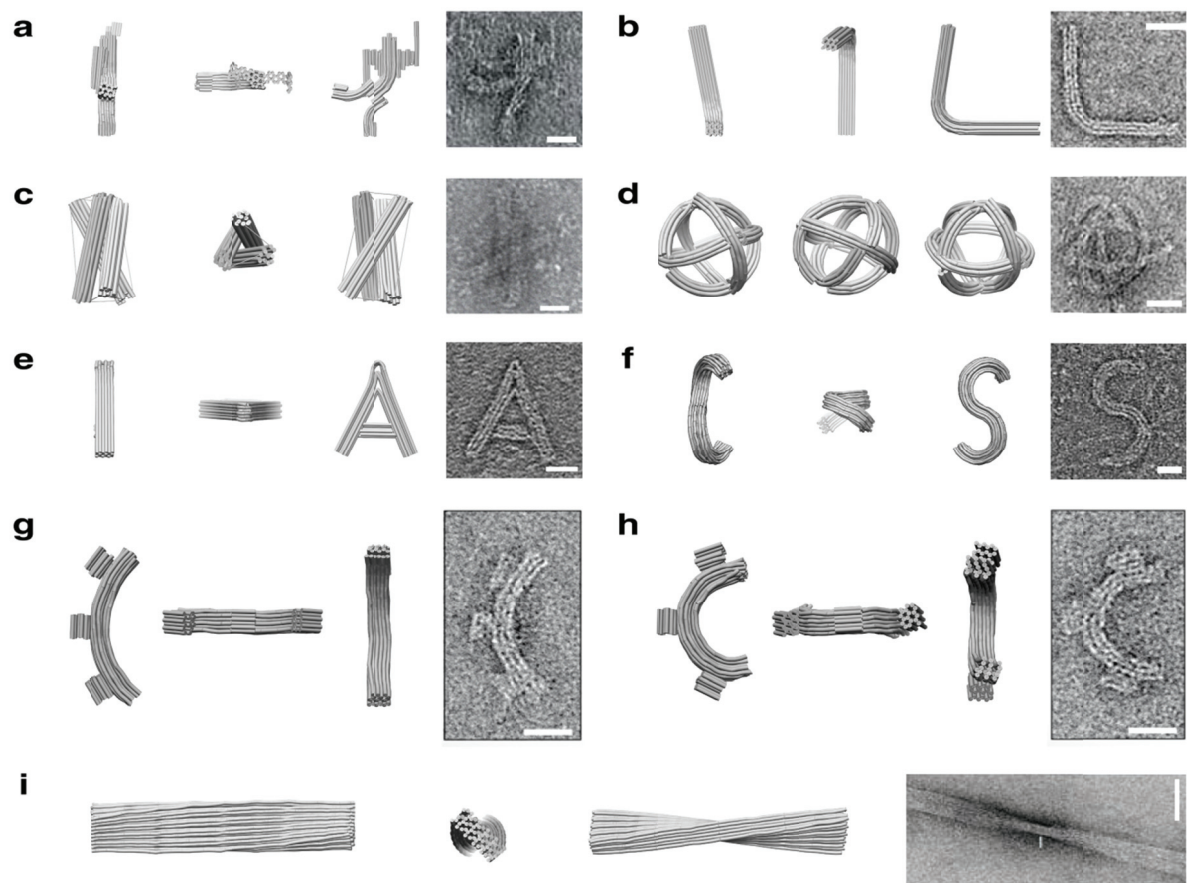


Figure S9 Experimental validation of nonlinear solution shapes predicted for a variety of DNA nanostructures. 3D renderings of the predicted solution shapes in three orthogonal views with corresponding TEM images for various complex shapes including (a) robot-like object (1), (b) bent bar (7), (c) tensegrity prism (11), (d) spherical wireframe object (7), (e) ‘A’-like object, (f) ‘S’-like object, (g) 90° gear-like object (1,7), (h) 180° gear-like object (1,7), and (i) twisted ribbon (1,7). Scale bars correspond to 20 nm (a-h) and 50 nm (i). TEM images in (a), (g), and (h) are reprinted from (1). TEM images in (b), (d) and (i) are reprinted from (7). TEM image in (c) is reprinted by permission from Macmillan Publishers Ltd: *Nature Nanotechnology* (11), copyright (2010).



Figure S10 TEM images of the 32-helix bundle with a crossover spacing of 21 basepairs that exhibits a clear stripe pattern. The first two images correspond to the mean and variance of 69 single-particle images.

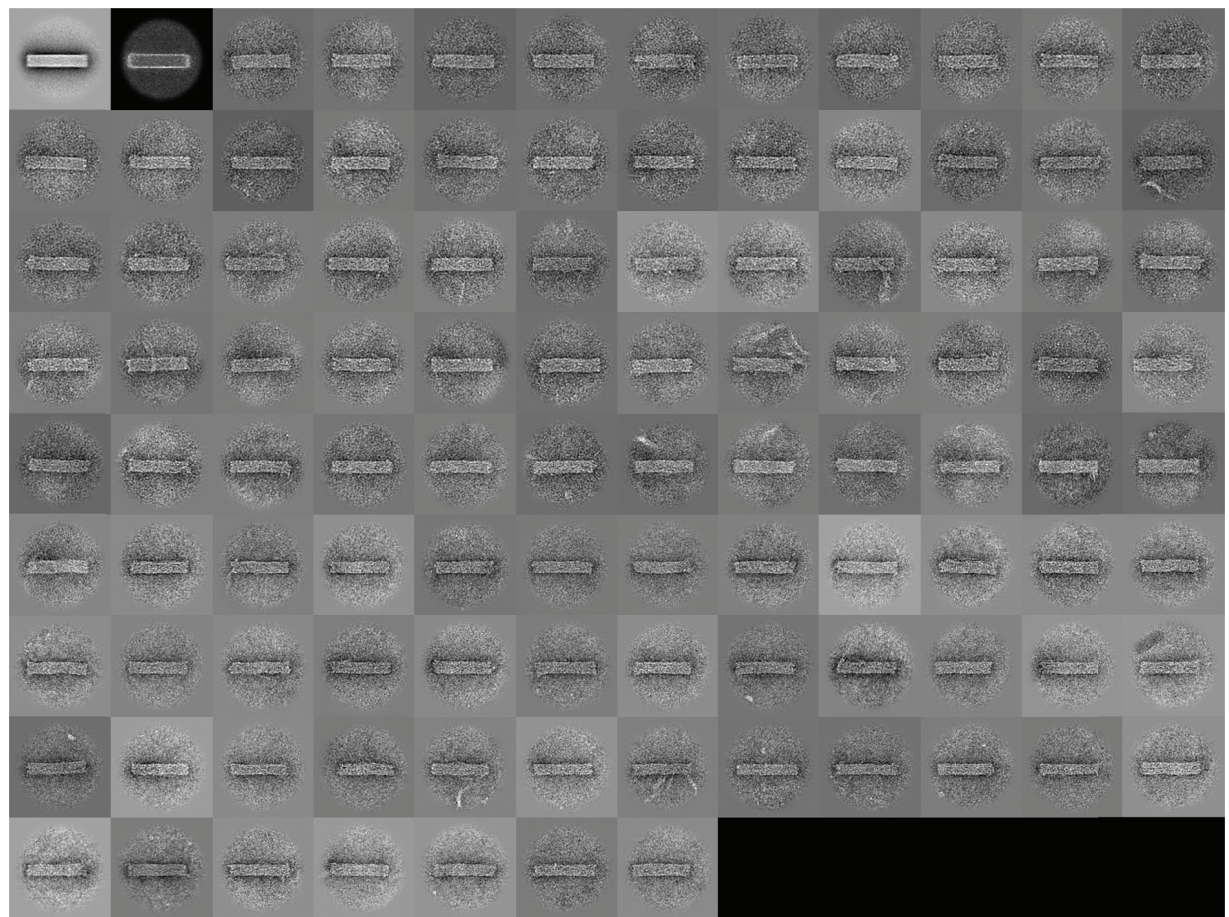


Figure S11 TEM images of the 32-helix bundle with a crossover spacing of 21 basepairs that does not exhibit a clear stripe pattern. The first two images show the mean and variance of 101 single-particle images.



Figure S12 TEM images of 32-helix bundle with crossover spacing of 42 basepairs. The first two images show the mean and variance of 130 single-particle images.

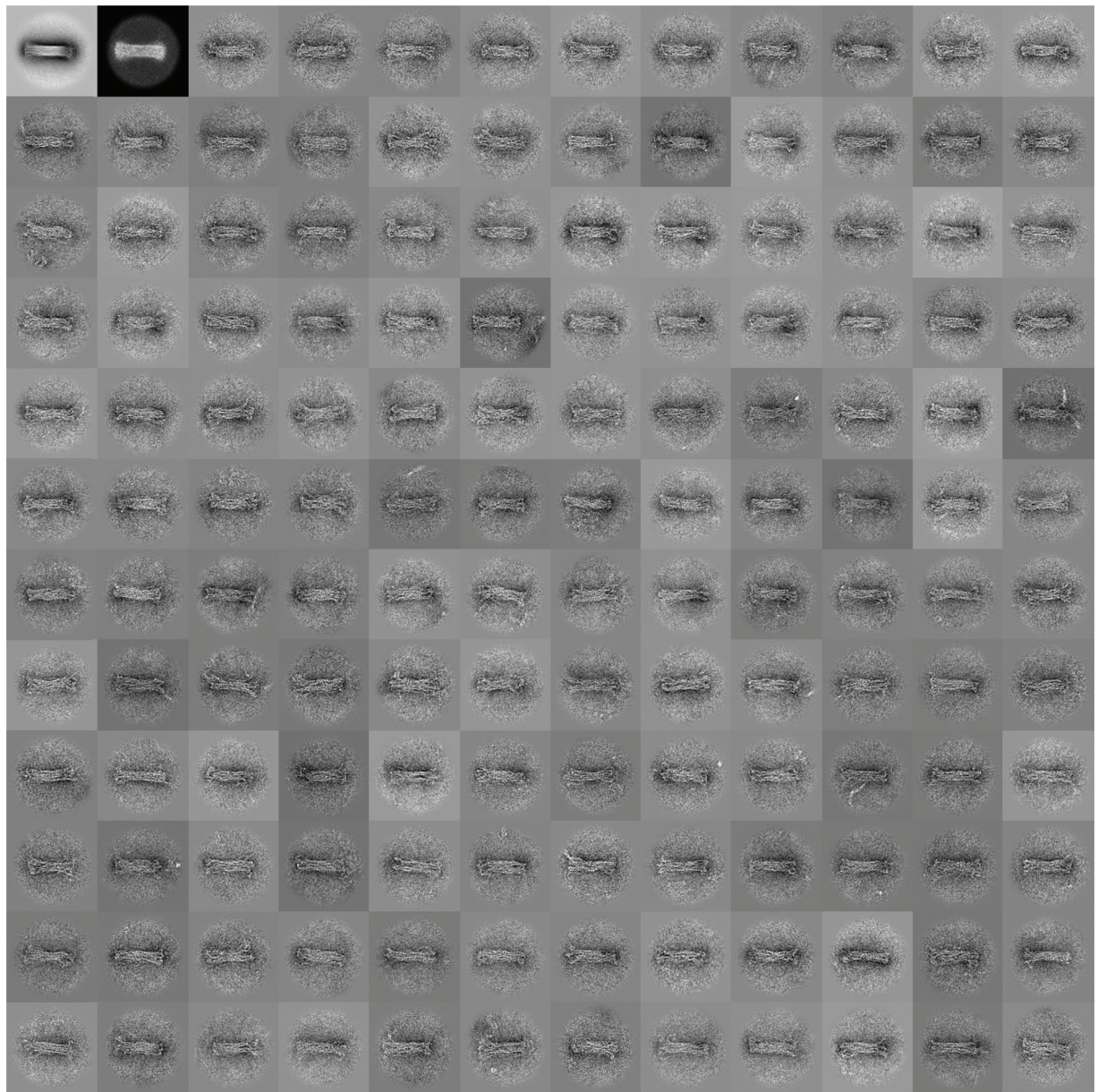


Figure S13 TEM images of the 32-helix bundle with a crossover spacing of 63 basepairs. The first two images show the mean and variance of 142 single-particle images.

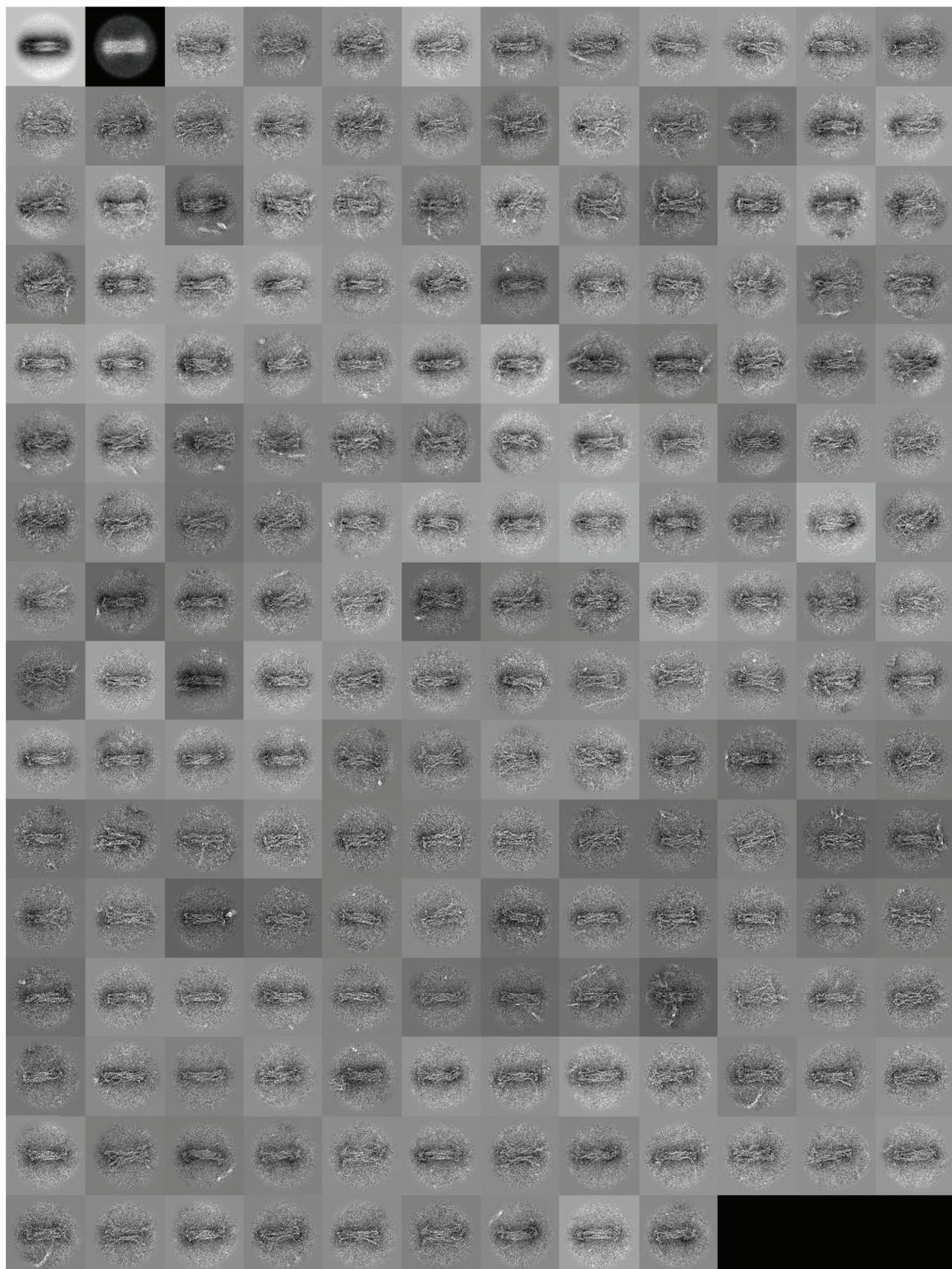


Figure S14 TEM images of the 32-helix bundle with crossover spacing of 84 basepairs. The first two images show the mean and variance of 187 single-particle images.

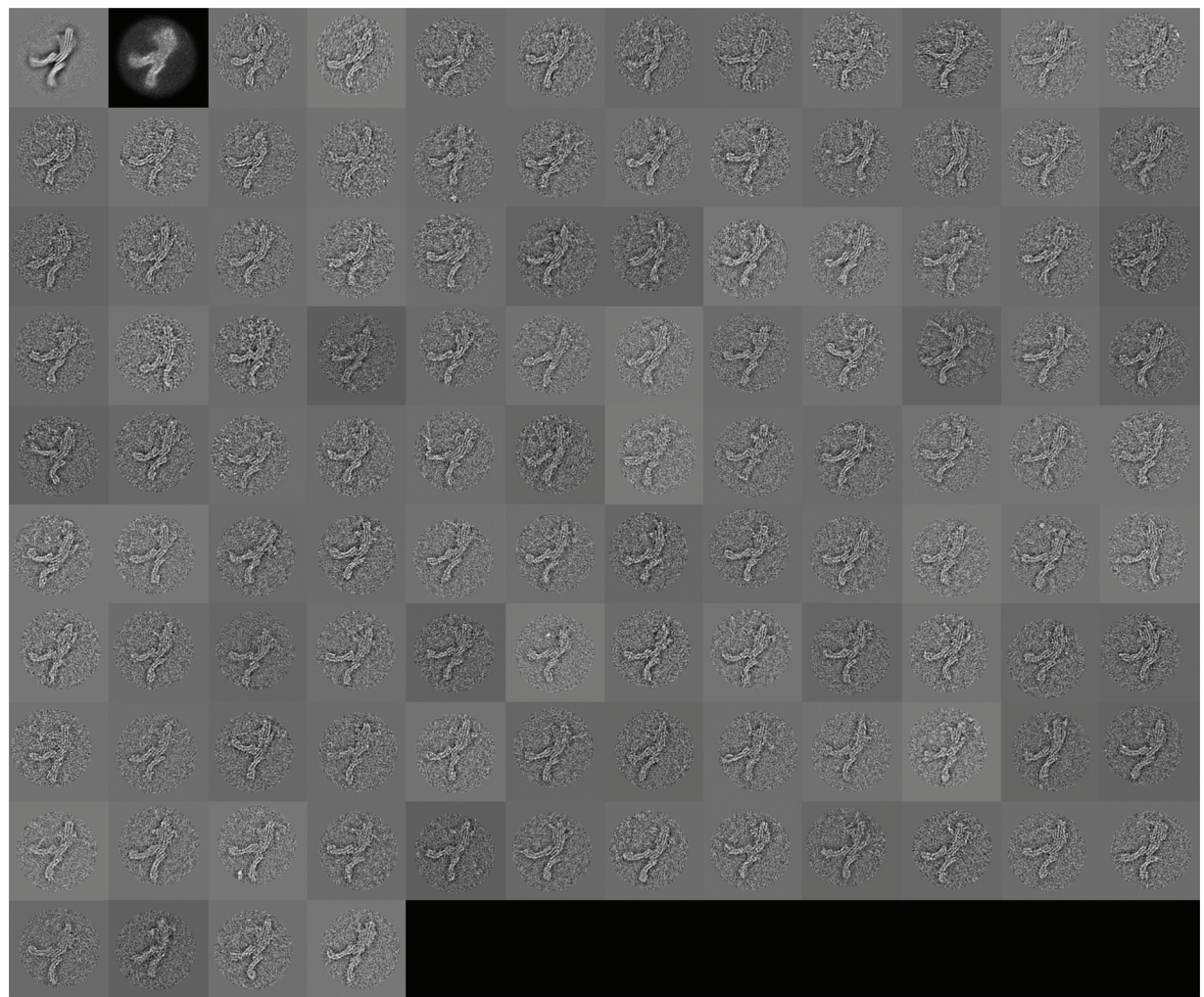
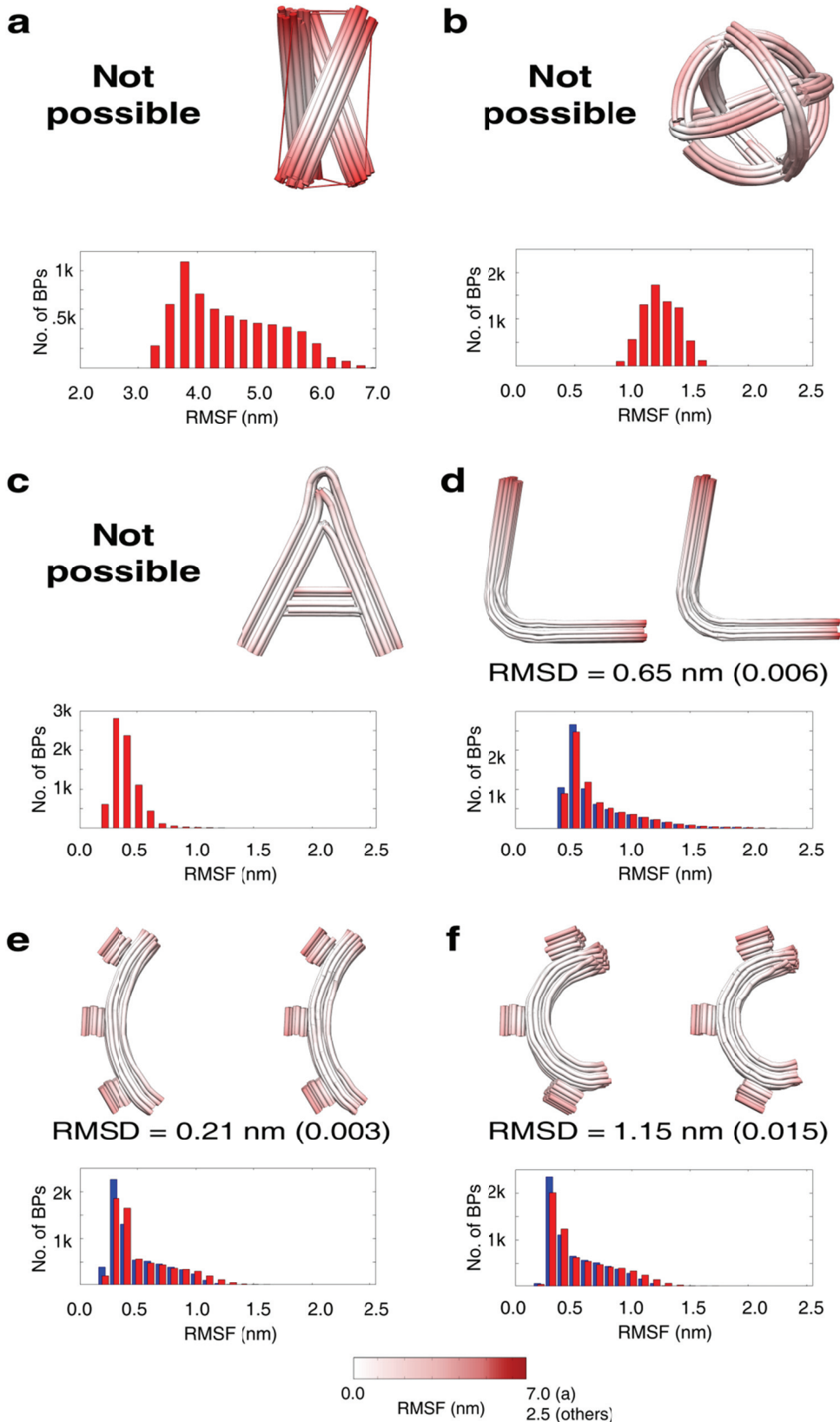
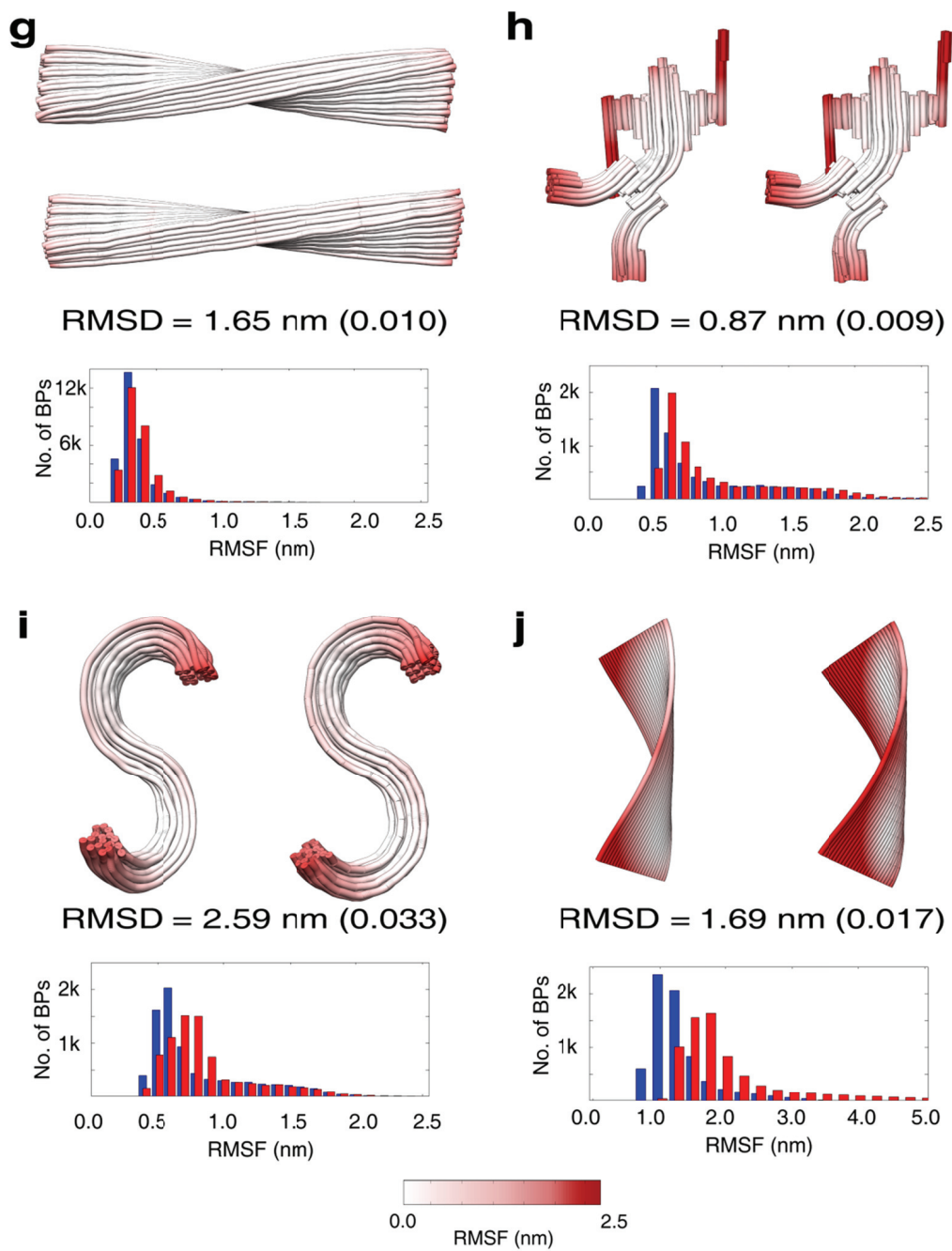


Figure S15 TEM images of the robot-like object. The first two images show the mean and variance of 110 single-particle images.





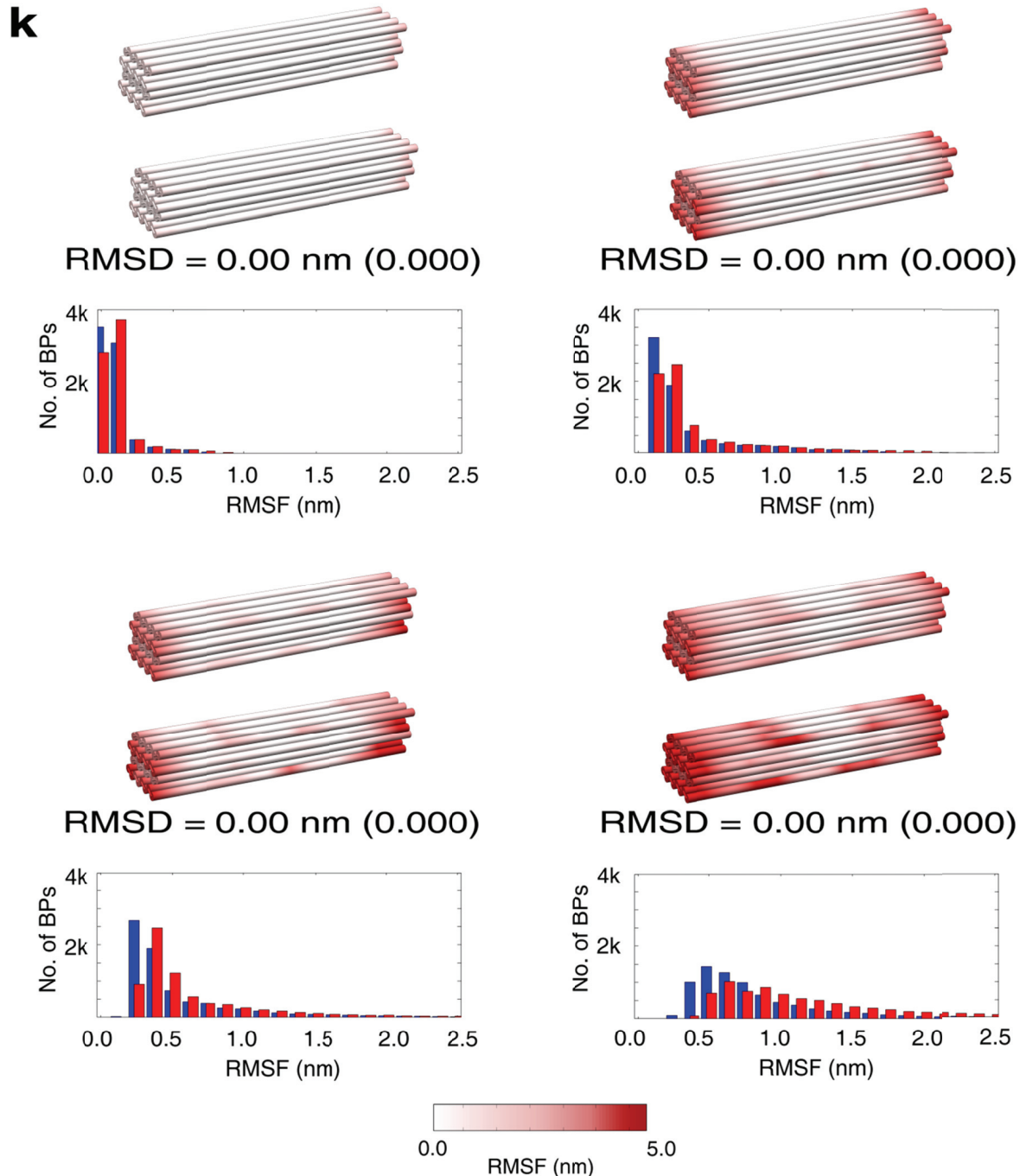


Figure S16 Comparison of solution shapes and flexibilities predicted by the old and current model for a variety of DNA nanostructures. (1st row) 3D renderings of the predicted solution shapes colored by root-mean-square fluctuation (RMSF) amplitude predicted by the old (top for g & k and left for others) and current model (bottom for g & k and right for others) and (2nd row) quantitative distributions in root-mean-square fluctuation amplitude from the old (blue) and current (red) model for (a) tensegrity prism

(11), (b) spherical wireframe object (7), (c) ‘A’-like object, (d) bent bar (7), (e) 90° gear-like object (1,7), (f) 180° gear-like object (1,7), (g) twisted ribbon (1,7), (h) robot-like object (1), (i) ‘S’-like object, (j) single-layer rectangular object (5), and (k) 32 helix bundle objects. RMSD represents root-mean-square distance between the predicted shapes of the old and current models. Values in parenthesis denote RMSD normalized by the maximum principal length of each structure, which is (d) 10.8, (e) 8.2, (f) 7.7, (g) 16.4, (h) 9.5, (i) 7.9, (j) 10.3, and (k) 7.9 nm. The tensegrity structure (a) and wireframe structures (b-c) could not be analyzed with the previous model (1). Predicted solution shapes do not change significantly with the new model, however RMSFs increase in some cases (h-k) due to the modeling of nicks that were previously ignored. Nicks did not affect the mean solution shape of the 32-helix bundles because no axial and torsional mismatch between neighboring DNA helices is present in these bundles. However, the effect of nicks on flexibility is more significant for bundles with lower crossover densities.

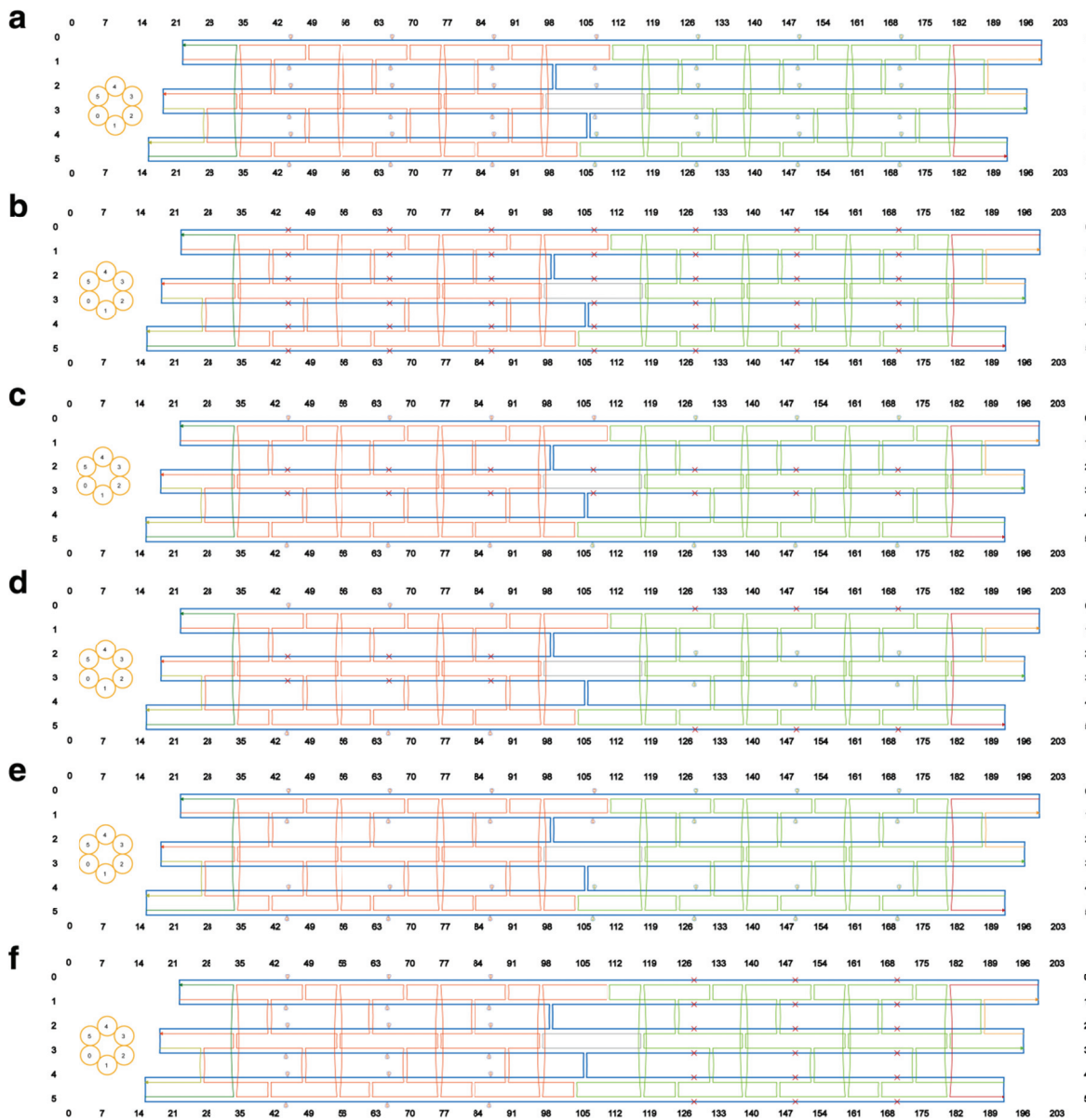


Figure S17 Scaffold and staple layout of the 6-helix bundles. Corresponding 3D solution shapes are (a) top left figure of Figure 1b, (b) bottom left figure of Figure 1b, (c) right figure of Figure 1b, (d) Supplementary Figure S2a, (e) Supplementary Figure S2b, and (f) Supplementary Figure S2c. Produced using caDNAno v1.0.

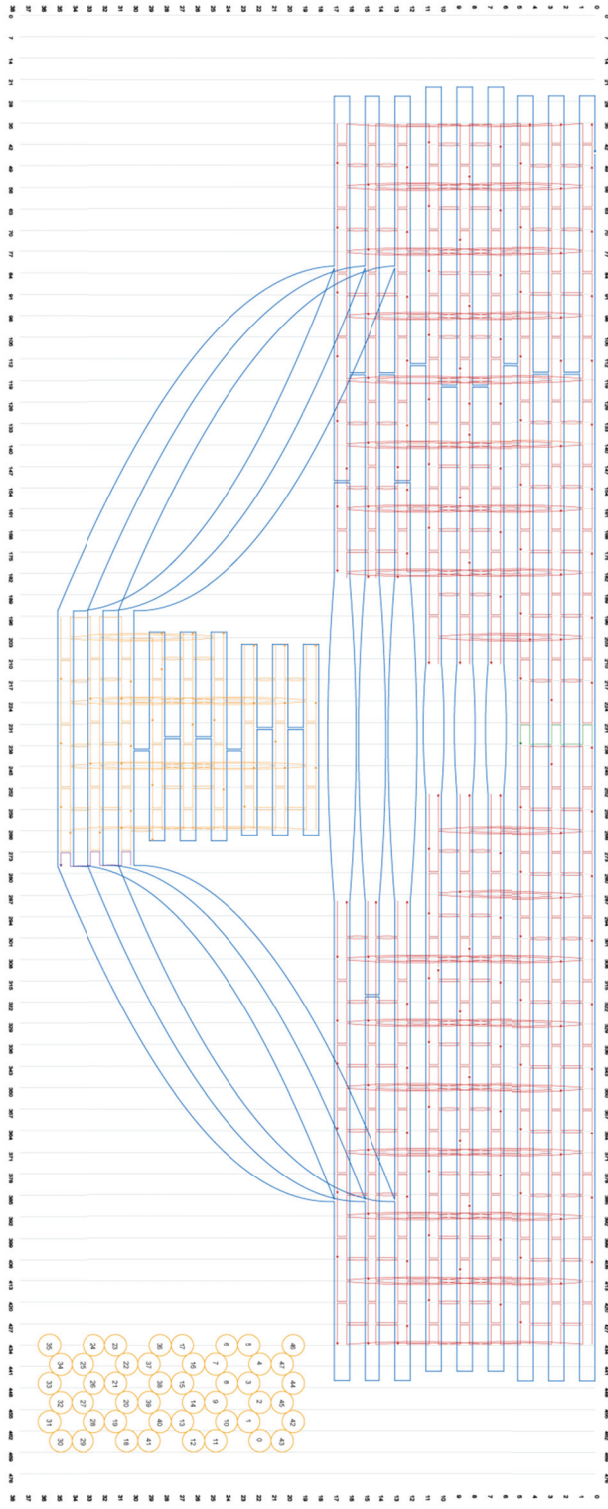


Figure S18 Scaffold and staple layout of the ‘A’-like object. Produced using caDNAno v1.0.

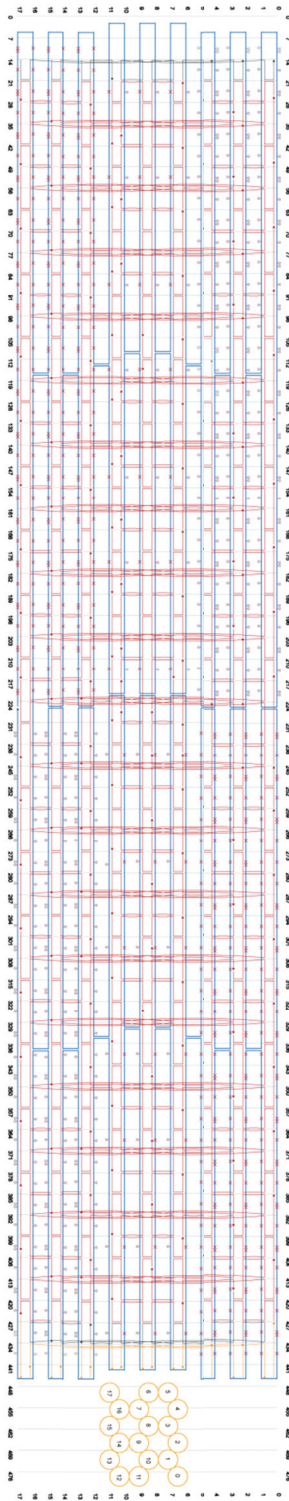


Figure S19 Scaffold and staple layout of the ‘S’-like object. Produced using caDNAno v1.0.

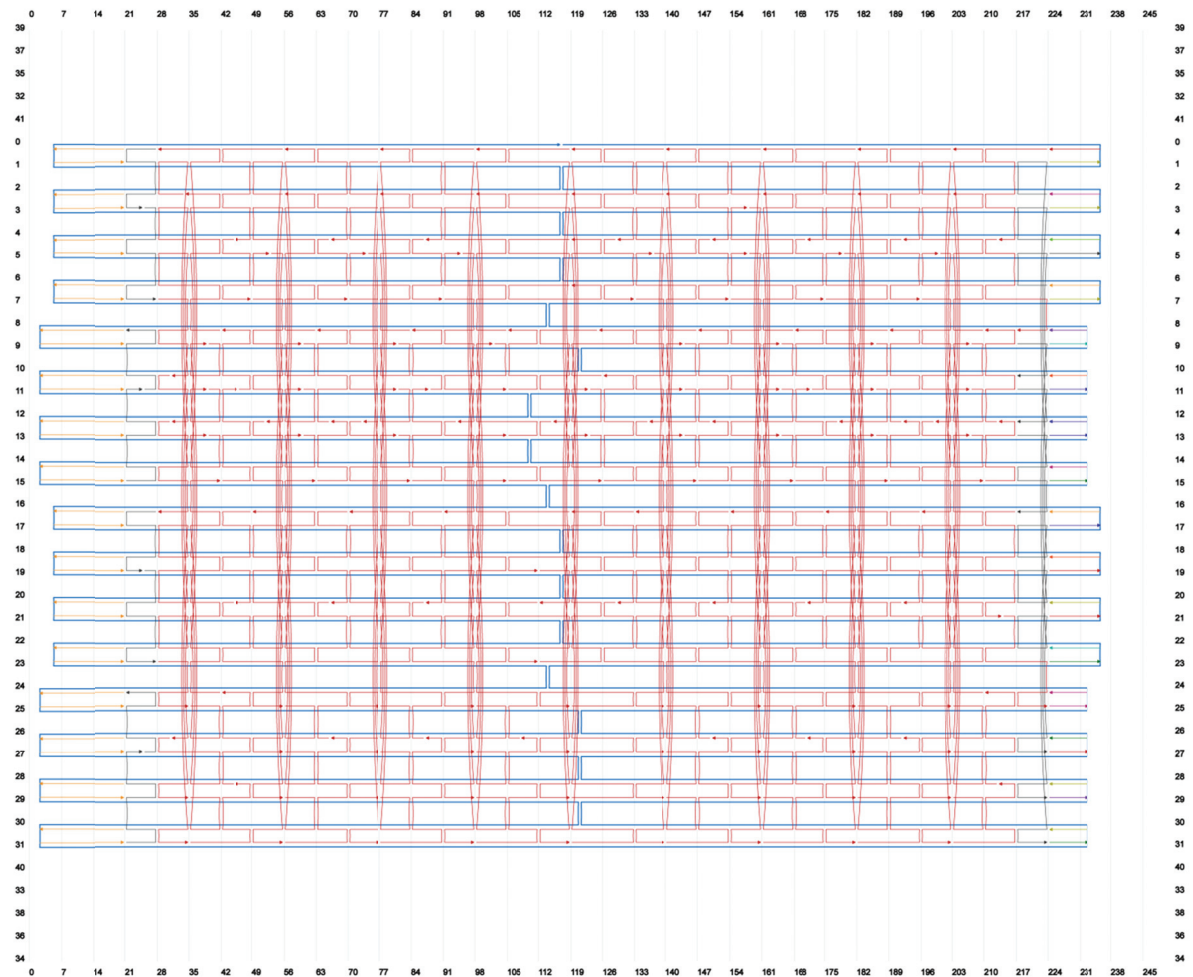


Figure S20 Scaffold and staple layout of the 32-helix bundle with crossover spacing of 21 basepairs.
Produced using caDNAno v1.0.

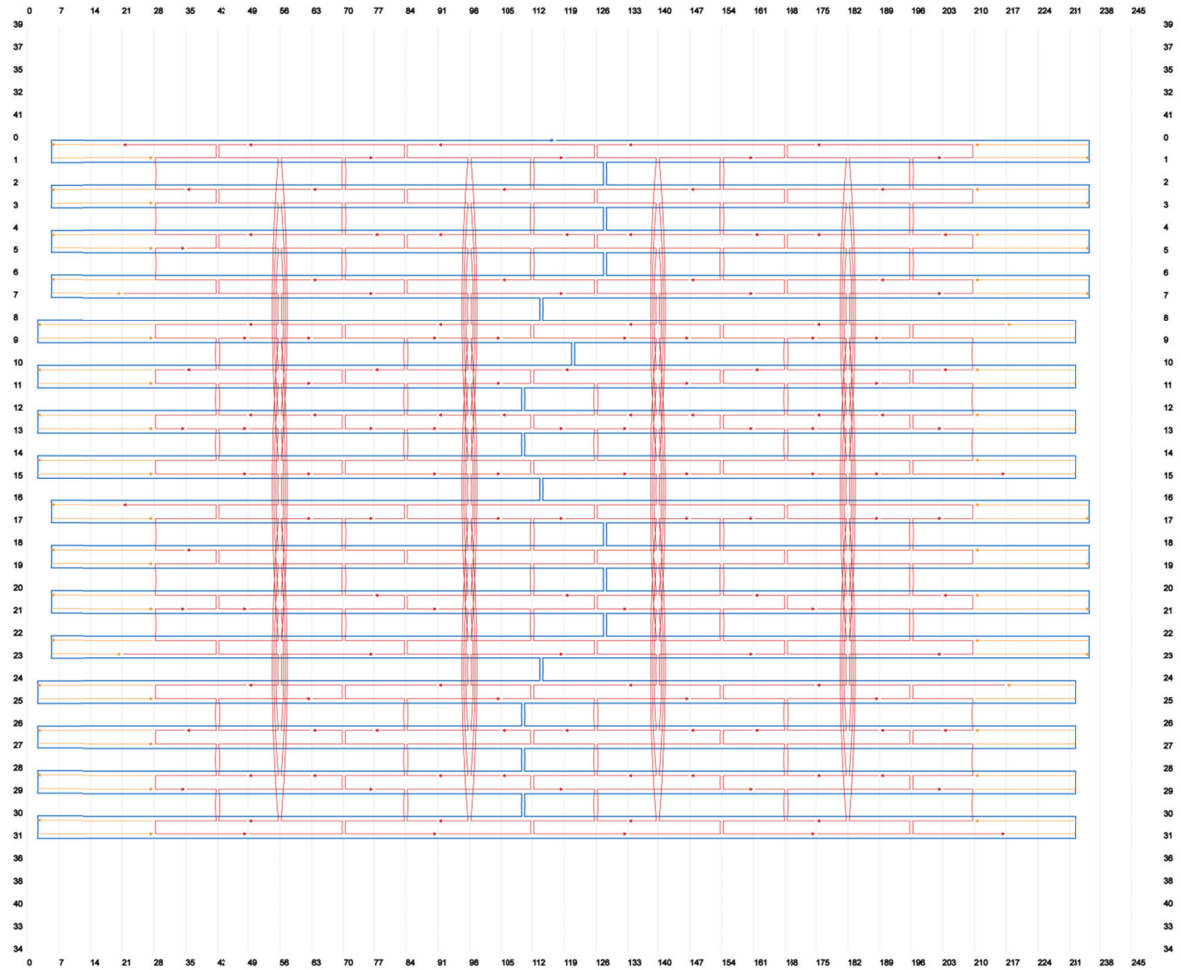


Figure S21 Scaffold and staple layout of the 32-helix bundle with crossover spacing of 42 basepairs.
Produced using caDNAno v1.0.

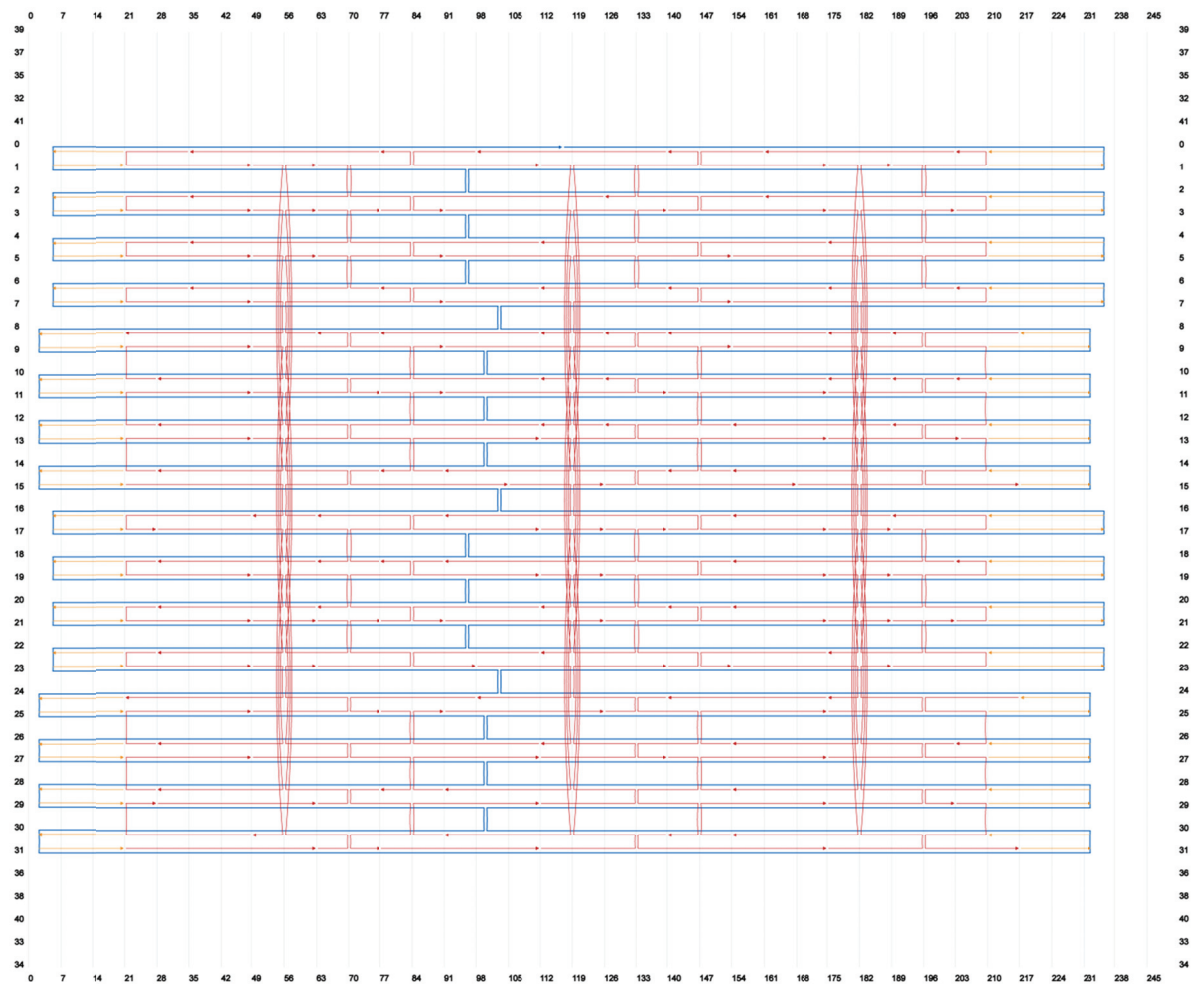


Figure S22 Scaffold and staple layout of the 32-helix bundle with crossover spacing of 63 basepairs.
Produced using caDNAno v1.0.

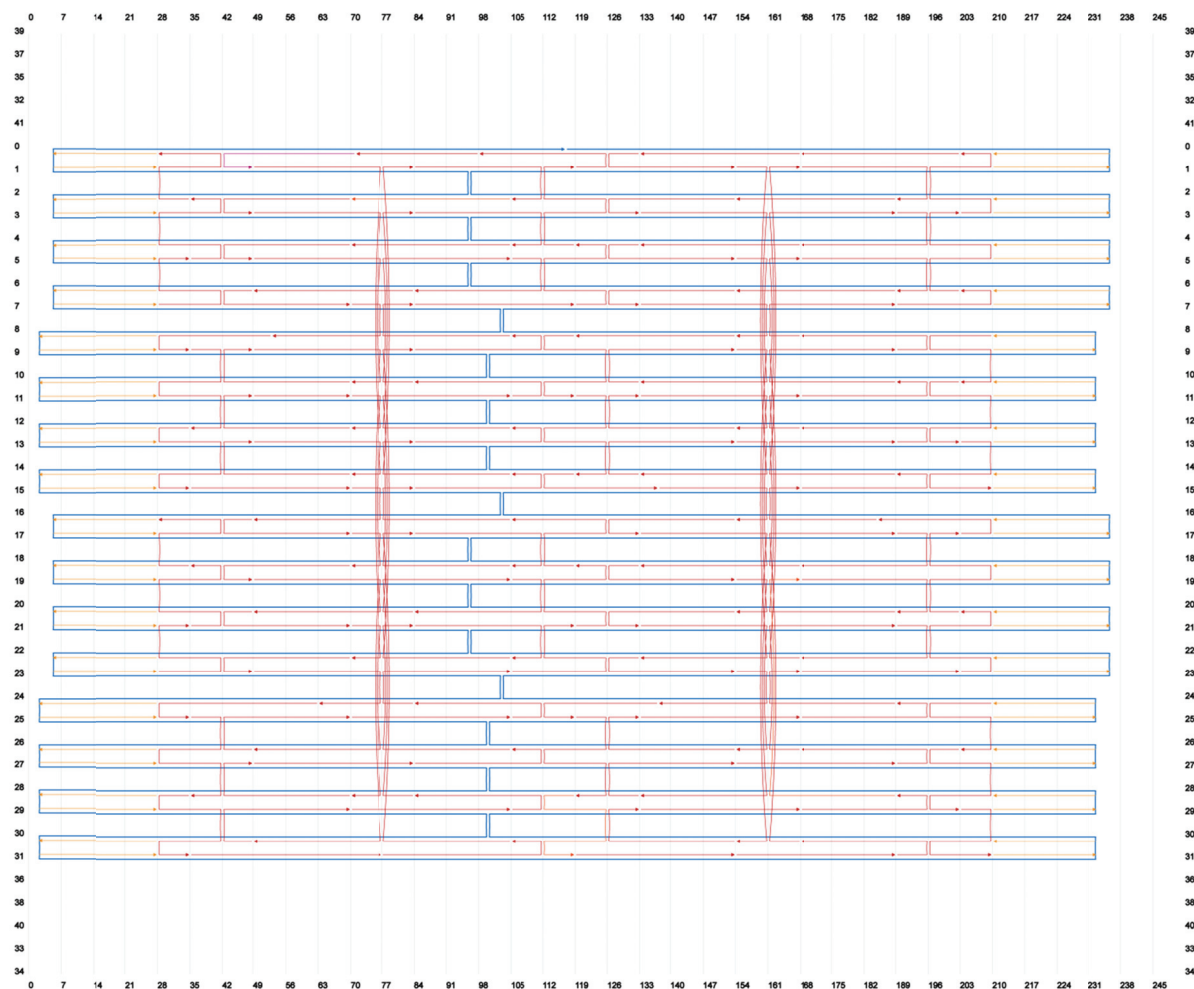


Figure S23 Scaffold and staple layout of the 32-helix bundle with crossover spacing of 84 basepairs.
Produced using caDNAno v1.0.